CHEMISTRY OF MATERIALS
Cite This: Chem. Mater. 2019, 31, 1981−1989
Article
pubs.acs.org/cm

Tetragonal $Cs_{1.17}In_{0.81}Cl_3$: A Charge-Ordered Indium Halide Perovskite Derivative

Xiaoyan Tan,[‡,†] Peter W. Stephens,[∥] Mylène Hendrickx,[⊥] Joke Hadermann,[⊥] Carlo U. Segre,[#] Mark Croft,[§] Chang-Jong Kang,[§] Zheng Deng,[▽] Saul H. Lapidus,[○] Sun Woo Kim,[◆] Changqing Jin,[▽] Gabriel Kotliar,[*,§] and Martha Greenblatt[*,‡]

[‡]Department of Chemistry and Chemical Biology and [§]Department of Physics and Astronomy, Rutgers, The State University of New Jersey, Piscataway, New Jersey 08854, United States

[∥]Department of Physics and Astronomy, State University of New York, Stony Brook, New York 11794, United States

[⊥]EMAT, University of Antwerp, Groenenborgerlaan 171, B-2020 Antwerp, Belgium

[#]Department of Physics and CSRRI, Illinois Institute of Technology, Chicago, Illinois 60616, United States

[▽]Institute of Physics, School of Physics, University of Chinese Academy of Sciences, Chinese Academy of Sciences, P.O. Box 603, Beijing 100190, P. R. China

[○]Advanced Photon Source, Argonne National Laboratory, Argonne, Illinois 60439, United States

[◆]Department of Chemical Education, Chosun University, Gwangju 61452, South Korea

S *Supporting Information*

ABSTRACT: Polycrystalline samples of $Cs_{1.17}In_{0.81}Cl_3$ were prepared by annealing a mixture of CsCl, InCl, and $InCl_3$, stoichiometric for the targeted $CsInCl_3$. Synchrotron powder X-ray diffraction refinement and chemical analysis by energy dispersive X-ray indicated that $Cs_{1.17}In_{0.81}Cl_3$, a tetragonal distorted perovskite derivative ($I4/m$), is the thermodynamically stable product. The refined unit cell parameters and space group were confirmed by electron diffraction. In the tetragonal structure, In^+ and In^{3+} are located in four different crystallographic sites, consistent with their corresponding bond lengths. In1, In2, and In3 are octahedrally coordinated, whereas In4 is at the center of a pentagonal bipyramid of Cl because of the noncooperative octahedral tilting of $In4Cl_6$. The charged-ordered In^+ and In^{3+} were also confirmed by X-ray absorption and Raman spectroscopy. $Cs_{1.17}In_{0.81}Cl_3$ is the first example of an inorganic halide double perovskite derivative with charged-ordered In^+ and In^{3+}. Band structure and optical conductivity calculations were carried out with both generalized gradient approximation (GGA) and modified Becke−Johnson (mBJ) approach; the GGA calculations estimated the band gap and optical band gap to be 2.27 eV and 2.4 eV, respectively. The large and indirect band gap suggests that $Cs_{1.17}In_{0.81}Cl_3$ is not a good candidate for photovoltaic application.

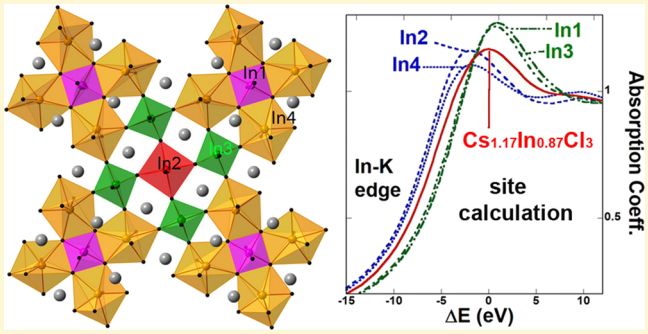

INTRODUCTION

Recently, inorganic halide perovskites and related compounds have gained attention because of their promising application in optoelectronic devices such as photodetectors, solar cells, light-emitting diodes, semiconductor lasers, and so forth.[1−9] In particular, cesium-based halide perovskites with formula $CsMX_3$ (M = Pb, Sn; X = Cl, Br, I) have shown exceptional optoelectronic properties. $CsPbI_3$ quantum dots have been incorporated into solar cells, which display a power conversion efficiency of 10.77%.[10] The efficiency can be further increased to 11.33% in $CsPb_{0.9}Sn_{0.1}IBr_2$ by substituting Pb with Sn and I with Br.[11] The highest efficiency of solar cells based on $CsPbI_3$ quantum dot films reaches 13.45%, which is the highest among all quantum-dot-based solar cells.[12] $CsPbBr_3$-based green light-emitting diodes exhibit a high electroluminescence quantum efficiency of 10.4%, which are the highest in all perovskite green light-emitting diodes.[13]

$CsPbX_3$ has outstanding properties but because of the toxicity of Pb, both experimental and theoretical scientists are searching for alternative inorganic halide perovskites. Filip et al. used computational screening methods and explored the possible cesium metal halide perovskites with other divalent metal ions such as Mg^{2+}, V^{2+}, Mn^{2+}, Ni^{2+}, Cd^{2+}, Hg^{2+}, Ga^{2+}, and In^{2+}.[14] The proposed $CsInCl_3$ and $CsInBr_3$ compounds are of interest because of the unusual 2+ valence state of In, which has not been reported so far. Later, Körbel et al. also carried

Received: November 15, 2018
Revised: February 17, 2019
Published: February 19, 2019

DOI: 10.1021/acs.chemmater.8b04771
Chem. Mater. 2019, 31, 1981−1989

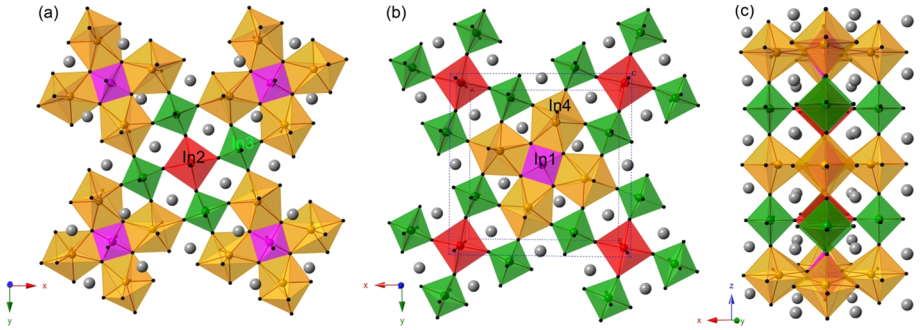

Figure 1. Crystal structure of $Cs_{1.17}In_{0.81}Cl_3$ with the space group $I4/m$. (a) The xy layer at $z = 0$, (b) the xy layer at $z = {}^1/_2$, and (c) a perspective view of the structure viewed along the y axis. Color code: In1 = magenta, In2 = red, In3 = green, In4 = orange, Cs = grey, and Cl = black.

out extensive density functional theory (DFT) calculations to explore novel inorganic perovskites and identified $CsInCl_3$ and $RbInBr_3$ as small gap semiconductors.[15] More recent work by Kang and Kotliar studied systematically the structures of $AInX_3$ compounds (A = alkali metals, X = F or Cl) and identified the low-lying structures of these materials and showed that $CsInCl_3$ should be thermodynamically stable and thus should form, providing further motivation for our studies.[16] Recent experimental study of the similar compound $CsTlX_3$ (X = F, Cl) found that Tl disproportionated into Tl^+ and Tl^{3+}.[17] Therefore, we expected that In might disproportionate into In^+ and In^{3+} in $CsInCl_3$ as well. To explore the existence of $CsInCl_3$ compound, its crystal structure, and the oxidation states of In, we embarked on the experimental work to synthesize and investigate the properties of $CsInCl_3$.

Another motivation for studying $CsInCl_3$ arises from its possible superconductivity, observed in related compounds. An example is the well-known perovskite $BaBiO_3$, an insulator with mixed valence Bi^{3+} and Bi^{5+}, which becomes superconducting by hole doping in $Ba_{0.6}K_{0.4}BiO_3$, and $BaBi_{0.7}Pb_{0.3}O_3$ because of the strongly phonon-coupled bands across the Fermi level.[18,19] $CsTlX_3$ has the same valence electron count as $BaBiO_3$, which is expected to show a similar band structure.[20] Theoretical calculations predict the superconducting critical temperatures of doped $CsTlF_3$ and $CsTlCl_3$ to be ∼30 and ∼20 K, respectively.[21] Although experimental work on $CsTlX_3$ has not yet discovered the superconductivity in these phases so far, it is of interest to explore analogous $CsInCl_3$ for future discovery.

In this manuscript, we report that polycrystalline $Cs_{1.17}In_{0.81}Cl_3$ can be prepared by conventional solid-state techniques. The crystal structure has been determined by X-ray and electron diffraction. The space group is $I4/m$, a distorted derivative of a cubic perovskite (Figure 1). The oxidation state of In is revealed by X-ray absorption spectroscopy. The band gap is determined by first-principles calculations and compared with literature results.[14,15]

EXPERIMENTAL METHODS

Starting Materials and Synthesis. The nominal $CsInCl_3$ phase was prepared by conventional solid state methods, similar to ones used for tetragonal $CsTlCl_3$ ($I4/m$),[17] with anhydrous CsCl (wt 99.9%, Alfa Aesar), InCl (wt 99.995%, Alfa Aesar), and $InCl_3$ (wt 99.999%, Alfa Aesar). The starting materials were mixed in the ratio of $CsCl:InCl:InCl_3 = 2:1:1$, ground thoroughly, and loaded into a silica tube, which was sealed under vacuum ($<10^{-2}$ mbar). The ampule was ramped up to 923 K within 24 h, kept at this temperature for 24 h, and then cooled down to room temperature over a course of 24 h. All sample preparations were carried out in an Ar-filled glove box with O_2 and H_2O concentration below 1 ppm.

Laboratory and Synchrotron Powder X-ray Diffraction (SPXD). Samples were measured in the 2Θ range from 10 to 80° and collected for 1 h on a Bruker D8 Advance diffractometer (Cu Kα, λ = 1.5418 Å) with a SOL-X solid state detector. Room temperature SPXD (λ = 0.412723 Å) was collected in the 2Θ range from 0.5 to 50° at the 11-BM-B beam line at the Advanced Photon Source (APS), Argonne National Laboratory. Diffraction data analysis and Rietveld refinement were performed with TOPAS-Academic.[22]

Chemical Analysis. The chemical composition of the samples was determined by energy dispersive X-ray (EDX) analysis with a JEOL 5510 scanning electron microscope (SEM) equipped with an INCA system (Oxford Instruments). Sample preparation was carried out in the glove box to avoid contact with air. The powder was gently smeared out over carbon tape, which was mounted on a metal stub. The stub was transported to the SEM instrument in a protective Ar atmosphere. During insertion, the sample had to be exposed to air for a short while (maximum 5 min). Cs L, In L, and Cl K lines were used for the composition quantification.

A separate chemical composition analysis was performed on a FEI Osiris transmission electron microscope (TEM), operated at 200 kV equipped with a Super-X detector. A vacuum transfer holder was used to avoid contact with air, and the Cs L, In L, and Cl K lines were used for the composition quantification.

Electron Diffraction. The samples for the TEM analysis were prepared in the glove box by crushing the powder of the sample and gently depositing the dry powder on a copper grid covered with a holey carbon film. The sample was transported and inserted into the TEM without contact with air with a vacuum transfer holder. Selected area electron diffraction (SAED) patterns were performed with a FEI Tecnai G2 TEM.

Thermogravimetric Analysis (TGA) and Differential Scanning Calorimetry (DSC). A powder sample of about 25 mg was loaded into an alumina crucible in a SDT Q600 TA instrument and measured between room temperature and 1000 °C at a heating and cooling rate of 10 °C/min under argon flow.

X-ray Absorption Spectroscopy (XAS). XAS data were collected at the indium K-edge in fluorescence at the Materials Research Collaborative Access Team (MRCAT)[23] insertion device beam line (Sector 10-ID) on a powder-filled Kapton capillary at room temperature. Data were normalized and background subtracted with Athena and IFEFFIT.[24,25] White line intensities were obtained with Fityk[26] with a Gaussian peak function plus an arctangent step (constrained to the peak energy).

Raman Spectroscopy. Micro Raman measurements have been carried out with an inVia Raman microscope (Renishaw) and excited with a solid-state laser (λ_{exc} = 532 nm).

DFT Calculations. The all-electron full-potential linearized augmented plane-wave (FLAPW) method implemented in WIEN2k[27] was adopted to calculate the electronic structure. A generalized gradient approximation (GGA) functional[28] was chosen to calculate the electronic structure. Because GGA underestimates a band gap, we used the modified Becke–Johnson (mBJ) exchange

DOI: 10.1021/acs.chemmater.8b04771
Chem. Mater. 2019, 31, 1981−1989

potential[29] to determine the precise band gap. A 17 × 17 × 17 k-mesh was used for the Brillouin zone integration, and the plane-wave cutoff was R_{mt} K_{max} = 7 in the calculations.

RESULTS AND DISCUSSION

Chemical Analysis and Crystal Structure. A polycrystalline light yellow product was obtained, and powder X-ray diffraction (PXD) analysis confirmed the major phase to be "$CsInCl_3$" with ∼5% of the $Cs_2InCl_5·H_2O$ impurity. The sample is hygroscopic, and the color of sample becomes darker when it is exposed to air. Numerous efforts to synthesize $CsInF_3$ and $RbInCl_3$ with similar approach at different temperatures failed to yield the targeted phases.

SEM-EDX and TEM-EDX measurements were carried out to investigate the chemical composition of the "$CsInCl_3$" product. Both EDX studies clearly confirm the presence of the Cs, In, and Cl elements (representative spectrum in Figure S1). The TEM-EDX study of 20 different crystals reveals a molar ratio of Cs:In:Cl = 0.26(2):0.18(1):0.56(2), which is close to a target of 1:1:3 but with an excess of Cs and less In. This is equivalent to a Cs/In ratio of 1.44 ± 0.14. These results are also confirmed by a statistical SEM-EDX study taken from 50 different crystals, which shows a molar ratio of Cs:In:Cl = 0.23(2):0.16(1):0.60(2) with a Cs/In ratio equal to 1.44 ± 0.16. Thus, the chemical analysis indicates that the composition of the material produced is a Cs rich, In deficient phase of formula $Cs_{1.17}In_{0.81}Cl_3$. We speculate that the difference from stoichiometry is not an intrinsic property of the nominal $CsInCl_3$ phase but due to unknown side reaction(s).

SPXD of the $Cs_{1.17}In_{0.81}Cl_3$ sample is very similar to that of $CsTlCl_3$, and indeed, initial Rietveld refinement results indicate that it is isostructural with tetragonal $CsTlCl_3$.[17] In this structure, shown in Figure 1, there are two Cs sites, four In sites, and seven Cl sites. The SEM-EDX results imply that there must be a significant amount of Cs in the nominal In sites as discussed below. Isotropic thermal parameters were refined independently for each site, except for those of the Cl sites, which had a common thermal factor. The Rietveld fit is shown in Figure 2, and the refined crystallographic data are summarized in Table 1. Details of the refinement, including raw data and computed fit, have been deposited as a cif file in the inorganic crystal structure database with CCDC number 1877027.

Two of the nominal In sites, In1 and In3, are octahedrally coordinated, with In−Cl distances between 2.50−2.64 Å, close to the value expected for the In^{3+}−Cl^- distances based on Shannon sum of radii (2.61 Å). The calculated bond valence values for the sum of In1 and In3 are 3.06 and 3.14, respectively.[30] Therefore, the charge of In on In1 and In3 sites can be assigned to 3+. The observed In^{3+}−Cl^- distances are also consistent with distances in $Cs_3In_2Cl_9$ (2.41−2.65 Å)[31] and $Cs_2InCl_5·H_2O$ (2.47−2.71 Å).[32]

The remaining two nominal In sites have significantly longer In−Cl bond distances (3.00−3.55 Å), indicating a lower oxidation state on In2 and In4 sites. On the basis of the similar bond distances between $Cs_{1.17}In_{0.81}Cl_3$ and $CsTlCl_3$ (Table 2), one would conclude that In^+ occupies In2 and In4 sites, similar to the case of Tl^+ on Tl2 and Tl4 sites. Although the Shannon radius of In^+ is not assigned, the estimated In^+−Cl^- distance should be close to the expected Tl^+−Cl^- distance (3.31 Å) for a six-coordinated environment, which agrees with In^+−Cl^- distances in $Cs_{1.17}In_{0.81}Cl_3$. The observed In^+−Cl^- distances

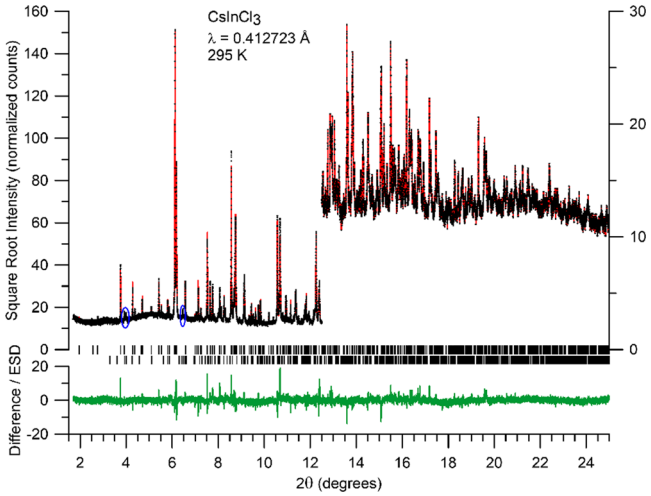

Figure 2. Rietveld refinement of synchrotron powder X-ray diffraction pattern of $Cs_{1.17}In_{0.81}Cl_3$, including ∼5% of the $Cs_2InCl_5·H_2O$ impurity. Black dots are the observed pattern, the red line is the calculated pattern, vertical black bars are the Bragg positions of $Cs_{1.17}In_{0.81}Cl_3$ (upper row) and $Cs_2InCl_5·H_2O$ impurity (lower row), and the green line is the difference between observed and calculated patterns. The most visible peaks of the impurity phase are circled in blue.

are also comparable with those in red InCl (2.87−3.26 Å) and yellow InCl (2.90−3.53 Å).[33] In2 is octahedrally coordinated, whereas In4 is at the center of a pentagonal bipyramid of Cl. It is therefore not surprising that $In4^+$−Cl^- distances (3.05−3.55 Å) are longer than $In2^+$−Cl^- distances (3.00−3.02 Å). The long $In4^+$−Cl^- distances are also observed in the mixed valence compound, In_5Cl_9, where the average In^+−Cl distance is 3.58 Å.[34] Thus, there is an In^+/In^{3+} charge order, no In^{2+} in $Cs_{1.17}In_{0.81}Cl_3$, similar to that of Tl^+/Tl^{3+} in $CsTl^+_{0.5}Tl^{3+}_{0.5}Cl_3$.

We now turn to the occupancy of the metal sites. If only In is placed in the In sites, refined occupancies in three of the sites are essentially unity and 0.93 ± 0.01 in site In2 for a sample composition of $CsIn_{0.996}Cl_3$. This refinement is presented as model I in Table S1. However, the EDX results imply that there must be a significant amount of Cs in sites that are nominally In. The X-ray diffraction essentially measures the total number of electrons (not only valence) in each atomic site, and so the Rietveld refinements are consistent with the replacement of unit occupancy of In by a fraction x Cs, (1−55/49x) In, and (1−6/49x) vacancies. (These estimates based on atomic number are borne out by refinements with the full atomic form factors, and they are not significantly affected whether one uses tabulated form factors for neutral atoms or ions). If we assume that Cs^+ only goes into the In^+ sites, that is, In2 and In4, and seeks to substitute enough Cs for In to account for the observed ratio of Cs:In, 1.44 ± 0.14, the problem of occupancy of sites In2 and In4 is still undetermined. The allowed parameter space, including standard uncertainties of the EDX and X-ray refinements, is illustrated in Figure S2. Table 1 describes a refinement of model II for a composition, $Cs_{1.17}In_{0.81}Cl_3$, with an equal ratio of Cs to In in each of the 1+ sites, 0.536, and a total ratio of Cs to In of 1.44; other assignments of occupancies, consistent with the parameters in Figure S2, give Rietveld fits that are essentially indistinguishable. The consequent vacancies in sites In2 and In4 (11 and 3%, respectively) create an apparent

DOI: 10.1021/acs.chemmater.8b04771
Chem. Mater. 2019, 31, 1981−1989

Table 1. Refined Crystallographic Data of $Cs_{1.17}In_{0.81}Cl_3$ According to Model II Described in the Text

compound	$Cs_{1.17}In_{0.81}Cl_3$
chemical formula, mol wt	$Cs_{1.17}In_{0.81}Cl_3$, 354.20
X-ray wavelength	λ = 0.412723 Å
lattice dimensions; unit cell volume	$a = b$ = 17.1098(1) Å, c = 11.0523(1) Å, $\alpha = \beta = \gamma$ = 90°; 3235.50(5) Å^3
space group	$I4/m$, #87
Z	20
Rietveld criteria of fit for powder diffraction refinements[a]	χ^2 = 2.77, R_{wp} = 9.85%, R_p = 7.43%, R_{exp} = 5.91%, R_{Bragg} = 5.21%
parameters refined	62
parameter restraints[b]	9

nominal atom, (valence charge)	site multiplicity and Wyckoff symbol	x	y	z	fractional occupancy model II	B_{iso}
Cs1 (+1)	4*d*	0	1/2	1/4	1	5.7(2)
Cs2 (+1)	16*i*	0.2108(1)	0.1091(1)	0.2773(1)	1	4.64(5)
In1 (+3)	2*a*	0	0	0	In: 1	1.4(1)
In2 (+1)	2*b*	1/2	1/2	0	In: 0.577(7) Cs: 0.309(4)	5.4(3)
In3 (+3)	8*h*	0.4073(2)	0.1966(2)	0	In: 1	2.32(6)
In4 (+1)	8*h*	0.0837(2)	0.2589(2)	0	In: 0.629(3) Cs: 0.337(2)	5.1(4)
Cl1 (−1)	4*e*	0	0	0.227(1)	1	3.27(7)
Cl2 (−1)	16*i*	0.0926(4)	0.3073(4)	0.2688(4)	1	3.27(7)
Cl3 (−1)	8*h*	0.1372(5)	0.0586(6)	0	1	3.27(7)
Cl4 (−1)	8*h*	0.3771(6)	0.0524(7)	0	1	3.27(7)
Cl5 (−1)	8*h*	0.2616(6)	0.2470(7)	0	1	3.27(7)
Cl6 (−1)	8*h*	0.1529(7)	0.4539(7)	0	1	3.27(7)
Cl7 (−1)	8*h*	0.4579(8)	0.3297(6)	0	1	3.27(7)

[a] $R_{wp} = \sqrt{\frac{\sum_i w_i(y_i^{calc} - y_i^{obs})^2}{\sum_i w_i(y_i^{obs})^2}}$, $R_{exp} = \sqrt{\frac{N-P}{\sum_i w_i(y_i^{obs})^2}}$, $R_p = \sqrt{\frac{\sum_i(y_i^{calc} - y_i^{obs})^2}{\sum_i(y_i^{obs})^2}}$, $\chi^2 = (R_{wp}/R_{exp})^2$, where y_i^{calc} and y_i^{obs} are the calculated and observed intensities at the ith point in the profile, the weight w_i is $1/\sigma^2$ from counting statistics, with the same normalization factor, N is the number of points in the measured profile, and P is the number of refined parameters. R_{exp} is the expected value of R_{wp} if the only deviation of the data from the model is due to statistical errors. [b] All Cl thermal parameters were restrained to be equal plus three restraints on In:Cs vacancy composition of In2 and In4 sites.

Table 2. Selected Bond Distances in $Cs_{1.17}In_{0.81}Cl_3$ and Tl−Cl Bond Distances in $CsTlCl_3$[17a]

bond	Cs−Cl distances (Å)	bond	In−Cl distances (Å)	bond	Tl−Cl[17] distances (Å)
Cs1−Cl4	3.59(1) × 4	In1−Cl1	2.50(1) × 2	Tl1−Cl3	2.45(3) × 4
Cs1−Cl2	3.66(1) × 4	In1−Cl3	2.55(1) × 4	Tl1−Cl2	2.56(3) × 2
Cs1−Cl6	3.89(1) × 4	In2−Cl7	3.00(1) × 4	Tl2−Cl1	2.99(3) × 2
Cs2−Cl3	3.42(1)	In2−Cl1	3.02(1) × 2	Tl2−Cl7	3.07(3) × 4
Cs2−Cl5	3.51(1)	In3−Cl7	2.44(1)	Tl3−Cl7	2.39(3)
Cs2−Cl6	3.56(1)	In3−Cl6	2.49(1)	Tl3−Cl2	2.62(1) × 2
Cs2−Cl7	3.64(1)	In3−Cl4	2.52(1)	Tl3−Cl4	2.69(3)
Cs2−Cl2	3.69(1)	In3−Cl2	2.56(1) × 2	Tl3−Cl6	2.71(3)
Cs2−Cl2	3.83(1)	In3−Cl5	2.64(1)	Tl3−Cl5	2.84(3)
Cs2−Cl7	3.93(1)	In4−Cl5	3.05(1)	Tl4−Cl5	2.82(3)
Cs2−Cl2	3.95(1)	In4−Cl4	3.08(1)	Tl4−Cl4	2.93(3)
Cs2−Cl5	3.97(1)	In4−Cl2	3.09(1) × 2	Tl4−Cl2	3.01(1) × 2
Cs2−Cl1	4.10(1)	In4−Cl3	3.20(1)	Tl4−Cl3	3.26(3)
Cs2−Cl4	4.29(1)	In4−Cl6	3.54(1)	Tl4−Cl6	3.45(3)
		In4−Cl3	3.55(1)	Tl4−Cl3	3.55(3)

[a] For each metal atom, bonds are listed in order of increasing length.

valence charge imbalance. The most plausible solution is that some fraction of In in those sites must be In^{3+} instead of In^{1+}.

In the tetragonal *ab* plane, $In2Cl_6$ octahedra corner share by four $In3Cl_6$ octahedra in fourfold axis symmetry, whereas $In1Cl_6$ octahedra edge-share with $In4Cl_7$ pentagonal bipyramids in the same fashion. Then, these two symmetric segments are connected by corner-sharing $In3Cl_6$ octahedra and $In4Cl_7$ pentagonal bipyramids. Layers centered with $In2Cl_6$ and $In1Cl_6$ octahedra are shown in Figure 1a,b, respectively. These two layers alternate every half a unit cell along the tetragonal c axis with a corner-sharing connection (Figure 1c). The fully occupied A-site Cs atoms are located in the space between these $In1Cl_6$, $In2Cl_6$, $In3Cl_6$, and $In4Cl_7$ polyhedra.

One interesting feature of $Cs_{1.17}In_{0.81}Cl_3$ is that $In4^+$ is seven-coordinated with Cl^- and forms an $In4Cl_7$ pentagonal bipyramid. The irregular coordination environment and the long bond distances for In^+ may be attributed to the almost doubly filled In 5s atomic orbital as shown in the study of binary indium bromides.[35−37] Interestingly, the lone pair $5s^2$

DOI: 10.1021/acs.chemmater.8b04771
Chem. Mater. 2019, 31, 1981−1989

electrons of $In2^+$ are not stereoactive, whereas those of $In4^+$ appear to be active; a lone pair distortion can be switched on or off by the environment and does not always distort in its vicinity. If we disregard for the moment the nonstoichiometric composition and presence of Cs in the In sites, nominal "$CsIn^{+}_{0.5}In^{3+}_{0.5}Cl_3$" could be understood as "$Cs_2In^{+}In^{3+}Cl_6$", a modified form of a double perovskite halide with a B site charge order in the formula of $A_2BB'X_6$.[38] In the double perovskite, the three-dimensional (3D) framework is formed by corner-sharing BX_6 and $B'X_6$ octahedra, with A site atoms occupying the cubo-octahedral void of the 3D structure. The modified double perovskite tetragonal structure ($I4/m$) of $Cs_{1.17}In_{0.81}Cl_3$ stems from the ~45° rotation in the ab plane of one-fifth of the $B'X_6$ octahedra ($In1Cl_6$) in the double perovskite structure.[39] This $In1Cl_6$ rotation results in the change of an adjacent In4 site coordination environment from $In4Cl_6$ octahedra to the $In4Cl_7$ pentagonal bipyramid, with long In4−Cl bond distances. Moreover, edge-sharing is created between $In1Cl_6$ and $In4Cl_7$. The interruption of connected corner-sharing caused by the $B'X_6$ octahedra rotation is defined as a noncooperative octahedral tilting (NCOT) in double perovskites.[40] Other examples in halides with a tetragonal structure ($I4/m$) include β-K_2KAlF_6, low temperature Rb_2KCrF_6, and β-Rb_2KGaF_6, in which the K ions on the B site are also coordinated with seven F atoms and form pentagonal bipyramids.[39,41] NCOT also has been reported in oxides and oxyfluorides.[42−44] In the modified double perovskite structure of $Cs_{1.17}In_{0.81}Cl_3$, the environment of A site ions is also change, where Cs1 still remains in the cubo-octahedral geometry, but Cs2 connects with eleven Cl and forms an irregular polyhedron (Figure 3).

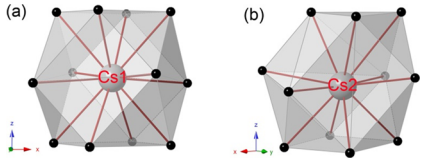

Figure 3. Coordination environment for (a) Cs1 and (b) Cs2 in $Cs_{1.17}In_{0.81}Cl_3$.

Electron Diffraction. To confirm the refined crystal structure based on SPXD data, selected area electron diffraction (SAED) patterns of the $Cs_{1.17}In_{0.81}Cl_3$ sample are taken from different zone axes ([100], [001], [$\bar{2}$10], [$\bar{1}\bar{1}$3]/[13$\bar{5}$], [35$\bar{3}$], and [4$\bar{2}\bar{5}$]) (Figure 4). All SAED patterns could be indexed with the tetragonal cell parameters: $a = b \approx 17.11$ Å, $c \approx 11.052$ Å, and $\alpha, \beta, \gamma = 90°$ and corresponded to the following reflection conditions: hkl: $h + k + l = 2n$; $hk0$: $h + k = 2n$; $0kl$: $k + l = 2n$; $0k0$: $k = 2n$.

To check the reflection condition $00l$ (whether it is $l = 2n$ or $l = 4n$), two tilt series of SAED patterns were obtained along the c-axis, shown in Figures S3 and S4. The intensity of the reflections $00l$: $l = 2n$ stays strong during the whole tilt series, indicating that they are not caused by double diffraction and thus do not corresponded to $00l$: $l = 4n$. According to the reflection conditions and cell parameters, the possible space groups are $I4$, $I\bar{4}$, $I4/m$, $I422$, $I4mm$, $I\bar{4}2m$, $I\bar{4}m2$, or $I4/mmm$.

On the basis of very clear intensity distributions in the reflections, all space groups with Laue class $4/mmm$ can be excluded. Here, we use the magnified experimental SAED pattern of the zone axis [001] for justification (Figure 5). In Figure 5, the projected positions of planes perpendicular to the

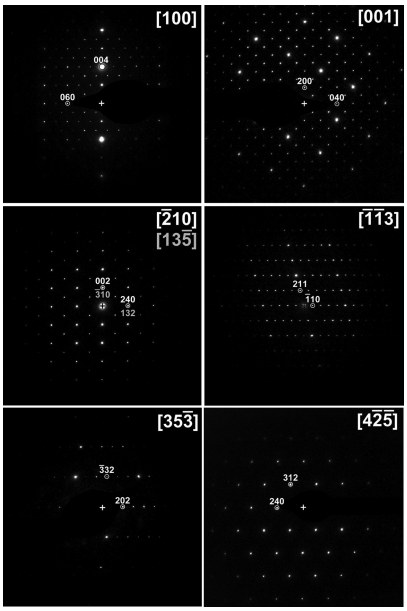

Figure 4. SAED patterns of the $Cs_{1.17}In_{0.81}Cl_3$ sample along the zone axes [100], [001], [$\bar{2}$10], [$\bar{1}\bar{1}$3]/[13$\bar{5}$], [35$\bar{3}$], and [4$\bar{2}\bar{5}$].

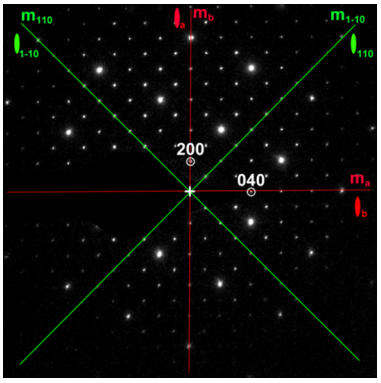

Figure 5. Magnified SAED pattern of zone axis [001]. The mirror plane perpendicular to x is indicated by "mx" and the twofold axis along x by an elliptical shape with index "x".

<a> and <110> directions and twofold axes along <a> and <110> are drawn. If these are mirror planes or twofold axes for the structure, the reflections connected by these symmetry elements should have equivalent intensities. It is clear that the intensity distribution of the reflections does not satisfy any of these symmetry elements. Therefore, this disagreement rules out all space groups with Laue class $4/mmm$, that is, $I422$, $I4mm$, $I\bar{4}2m$, $I\bar{4}m2$, or $I4/mmm$.

Sample Stability. The stability of the $Cs_{1.17}In_{0.81}Cl_3$ phase was determined by thermogravimetric analysis (TGA) and differential scanning calorimetry (DSC) between 300 and 1273 K under Ar flow. $Cs_{1.17}In_{0.81}Cl_3$ is thermally stable below 600 K without any phase transition or melting under the inert environment (Figure 6); however, the sample mass drops as the temperature increases from 600 to 1273 K. The mass drop between 600 and 900 K is probably due to sample melting. After 900 K, an endothermal peak shown in the DSC curve at 910 K indicates possible decomposition. The TGA−DSC curves are similar to those of tetragonal $CsTlCl_3$, which is thermally stable up to 623−673 K, the temperature where that phase also starts melting.

DOI: 10.1021/acs.chemmater.8b04771
Chem. Mater. 2019, 31, 1981−1989

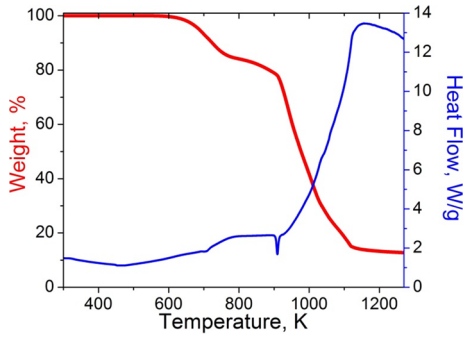

Figure 6. TGA–DSC measurement of $Cs_{1.17}In_{0.81}Cl_3$ between 298 and 1273 K.

X-ray Absorption Spectroscopy (XAS). As a p-block element, the frontier bonding orbitals of In are the 5p/5s states with the configurations: In^0 s^2p^1, In^{1+} s^2p^0 (reflecting the inert pair effect), and In^{3+} s^0p^0. X-ray absorption edges with final states in the p valence orbitals can be used to probe the valence/configuration of such p block elements. In Figure 7a, the In K near edge spectrum of $Cs_{1.17}In_{0.81}Cl_3$ is shown along with the standards: elemental In^0; In^{1+}, InCl; and In^{3+}, $InCl_3$, and In_2O_3.

The In K near edge spectra are dominated by a strong "white line" (WL) peak feature because of 2s core transitions into empty 5p states. This WL feature rides upon a step feature because of the onset of transitions into the continuum. Typically, two points regarding the In valence/WL feature coupling should be noted: first, the increase in WL intensity with increasing valence and second, the chemical shift of the WL to higher energy is not always consistent with increasing valence.[46−48] The chemical shifts in these materials appears to be too structure/ligand dependent for reliable interpretation, so the WL area will be focused upon.

The increased WL intensity, with increasing valence, is due partially to the increase of available empty p final states (e.g., between the In^0 and In^{1+} states) and partially due to the increased transition matrix element via the increased localization of the p final states upon loss of screening with increasing valence (e.g., the loss of the s^2 screening between the In^{1+} and In^{3+} states). The systematic WL intensity increase between In, InCl, and $InCl_3$ is clear. The WL intensity in In_2O_3 is also enhanced by an amount somewhat more than in $InCl_3$ indicating bonding/ligand dependence. It is important to note that the WL intensity of $Cs_{1.17}In_{0.81}Cl_3$ is intermediate between the In^{1+} and In^{3+} standards (the sizable ligand/structure dependence in the In^{3+} standards is qualification to this statement). The plot of the Gaussian fitted WL areas versus In formal valence for the standard compounds (referred to above) is shown in Figure 8 along with a linear fit to the standard area

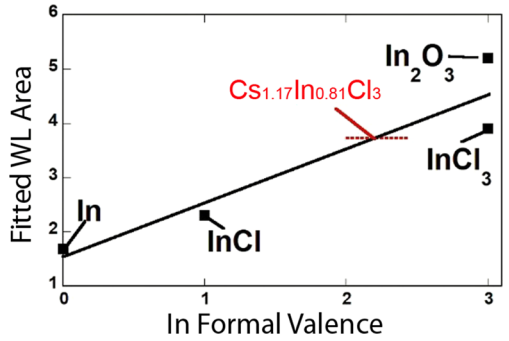

Figure 8. Plot of the Gaussian fitted WL area/intensity vs formal In valence for the In K edge standard spectra in Figure 7b. The solid line is a linear fit to the standard spectra data. The fitted WL area for $Cs_{1.17}In_{0.81}Cl_3$ is indicated by a dashed red line crossing the standard fitted line.

data. Within the nonnegligible uncertainties in these estimates, these results support the average valence in $Cs_{1.17}In_{0.81}Cl_3$ lying in the vicinity of In^{2+}.

As another check on the charge separation on the sites in $Cs_{1.17}In_{0.81}Cl_3$, FEFF 8.4 model[45] calculations for all of the sites were performed with the near-edge results being shown in Figure 7b. In view of the substantial uncertainty in absolute energy in such modeling, the results have been presented relative to the calculated all-site-average peak for $Cs_{1.17}In_{0.81}Cl_3$. The determined structure was used in this modeling. The model calculations indicate: the In2 and In4 sites have a smaller chemical shift and smaller WL area consistent with a smaller In valence and the In1 and In3 sites have a larger chemical shift and larger WL area consistent with

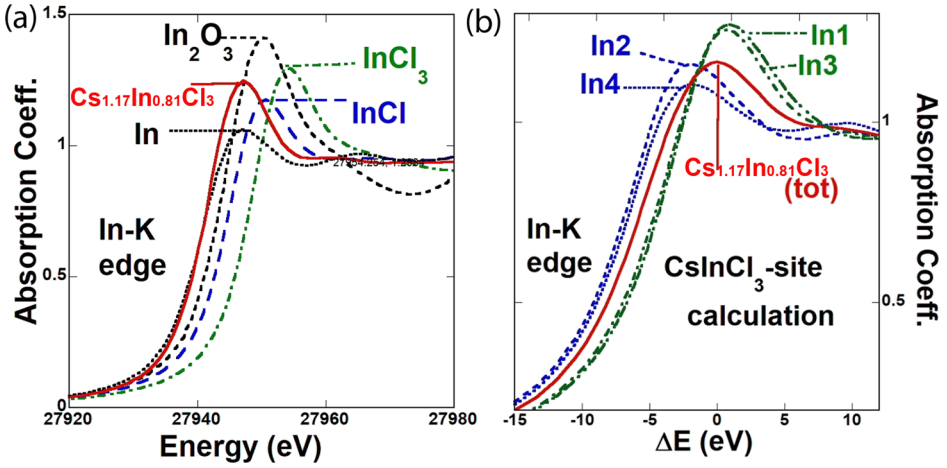

Figure 7. (a) Comparison of the In K edges of $Cs_{1.17}In_{0.81}Cl_3$ to those of the standards: In^0, In metal; In^{1+}, InCl; In^{3+}, $InCl_3$, and In_2O_3. (b) An FEFF 8.4 modeling[45] of the In K edges at the individual In1, In2, In3, and In4 sites as well as the all-site total $Cs_{1.17}In_{0.81}Cl_3$ spectrum. The energy ΔE is given relative to the all-site WL peak value.

DOI: 10.1021/acs.chemmater.8b04771
Chem. Mater. 2019, 31, 1981−1989

a larger In valence. Thus, the model results are consistent with the experimental observations. It is worth noting that charge separation in solids can often be smaller than the stable full integral valence differences.

Raman Spectroscopy. To further compare $Cs_{1.17}In_{0.81}Cl_3$ with $CsTlCl_3$ and $CsTl_{1-x}Hg_xCl_3$ ($0 \le x < 1$),[17,49] the Raman spectrum of $Cs_{1.17}In_{0.81}Cl_3$ was collected at room temperature under ambient pressure (Figure 9). For cubic $CsTlCl_3$, the

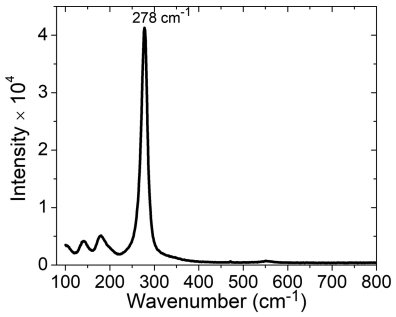

Figure 9. Raman spectrum of $Cs_{1.17}In_{0.81}Cl_3$ (λ_{exc} = 532 nm).

calculated phonon frequency of the Tl−Cl stretching mode is 277 cm^{-1}. The experimental Raman spectra of both cubic ($Fm\bar{3}m$) and tetragonal $CsTlCl_3$ ($I4/m$) show a major phonon frequency at 270 cm^{-1}, in agreement with the theoretical calculation results.[17] In $CsTl_{1-x}Hg_xCl_3$, active Raman Tl^+−Cl−Tl^{3+} modes are also observed around 270 cm^{-1}.[49] Here, the major phonon frequency of $Cs_{1.17}In_{0.81}Cl_3$ is at 278 cm^{-1}, which is close to values of Raman for Tl^+−Cl−Tl^{3+} modes in $CsTlCl_3$ and $CsTl_{1-x}Hg_xCl_3$. On the basis of the similarity observed in the structure and Raman spectra between $Cs_{1.17}In_{0.81}Cl_3$, $CsTlCl_3$, and $CsTl_{1-x}Hg_xCl_3$, the active Raman mode observed in $Cs_{1.17}In_{0.81}Cl_3$ can be ascribed to In^+−Cl−In^{3+}.

DFT Calculations. To gain insight of the band structure and estimate the band gap, first-principles DFT calculations were carried out with both GGA (PBE version) and mBJ approaches (Figure 10). The calculations were conducted on the $CsInCl_3$ version of the structural model I, that is, without considering the apparent presence of Cs in the In sites or attendant vacancies in the crystal structure of $Cs_{1.17}In_{0.81}Cl_3$. The band structure with GGA approaches the lowest energy of the conduction band located at the N point, whereas the highest energy of valence band is located at the X point, which indicates an indirect band gap of 2.27 eV (Figure 10a).

As shown in Figure 10, the valence band density of states (DOS) around the Fermi level is mostly contributed by the In states, but the strong peaks located at lower energy are dominated by Cl states (Figure 10a,b,d,e). The In2 (1+, $5s^2$) and In4 (1+, $5s^2$) 5s bands are located in valence bands, whereas In1 (3+, $5s^0$) and In3 (3+, $5s^0$) 5s bands are located in conduction bands, which clearly support the two oxidation states in the structure as revealed in the structure and XANES analysis. A broader computational survey of compounds $AInX_3$ (A = alkali metals, X = F or Cl) predicts that the most stable state of $CsInCl_3$, In has a single In^{2+} site, but that it is only slightly more likely to occur than the phase described in this work (Tables S2 and S3).[16]

GGA calculated corresponding optical conductivity predicts an optical gap of 2.42 eV (Figure 10c). In comparison with the GGA results, the calculated band structure using mBJ shows

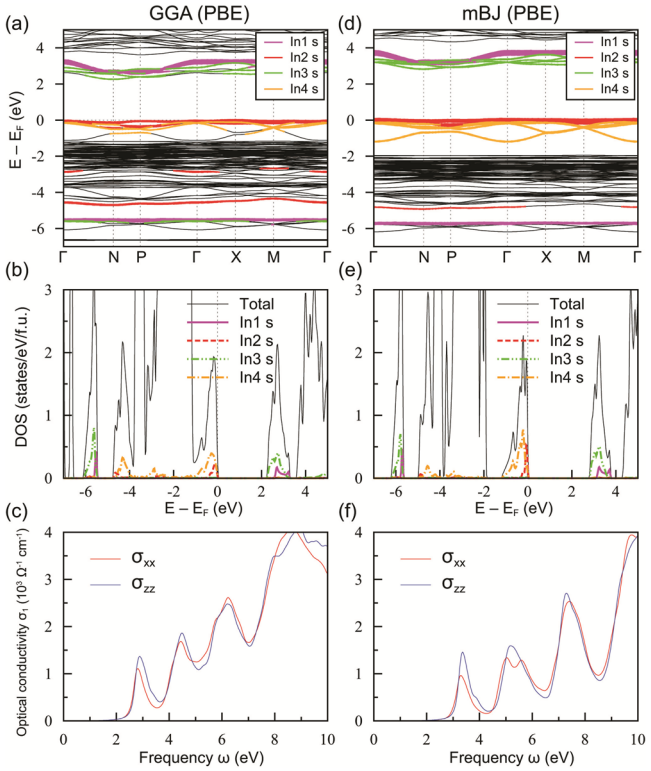

Figure 10. Band structure, density of states, and calculated optical conductivity of $CsInCl_3$ with (a, b, c) GGA and (d, e, f) mBJ.

similar indirect band gap features but with a larger band gap of 2.83 eV (Figure 10d−f). In the valence bands, these strong peaks are shifted to lower energy. Consequently, the calculated optical gap using the mBJ approach is increased to 3.03 eV. The calculated band gap here is much larger than the literature report (<1 eV) of theoretical $CsInCl_3$.[15] Because our calculations are carried out based on the experimental crystal structure, the estimated band gap shown here is more reliable than the reported values.[14,15] The total DOS and estimated optical band gap of $CsInCl_3$ are similar to those of $CsTlCl_3$,[17] which is predicted to exhibit superconductivity with proper doping. Therefore, it is worth carrying out further calculations and corresponding experiments on $CsInCl_3$ to explore the possibility of making it superconducting by design. It seems especially promising to seek the doping of this material, in view of its apparent natural tendency to prefer off stoichiometry. However, determining and controlling the charge state in sample preparation may be a significant challenge.

■ CONCLUSIONS

Although $CsInCl_3$ was originally predicted to be a perovskite, synchrotron X-ray diffraction data and X-ray fluorescence measurements show that the stable material has some Cs in the nominal In sites and adopts a tetragonal perovskite-related phase ($I4/m$) of composition $Cs_{1.17}In_{0.81}Cl_3$, with both corner-sharing and edge-sharing InCl6 octahedra and InCl7 pentagonal bipyramids. $Cs_{1.17}In_{0.81}Cl_3$ is isostructural with tetragonal $CsTlCl_3$, which was predicted to be a superconductor with proper doping. The revealed oxidation state of In is not 2+, as the theory predicted, but with a charge-ordering of In^+ and In^{3+} on four crystallographic positions in the structure. This is a rare inorganic compound accommodating both In^+ and In^{3+} in a nominally double perovskite-derived

DOI: 10.1021/acs.chemmater.8b04771
Chem. Mater. 2019, 31, 1981−1989

"$Cs_2In^+In^{3+}Cl_6$" structure. The mixed valence of In^+ and In^{3+} is confirmed by detailed X-ray absorption spectroscopy. Raman spectroscopy demonstrates the In^+−Cs−In^{3+} active mode with a phonon frequency of 278 cm^{-1}, similar to that of the Tl^+−Cs−Tl^{3+} stretching modes in $CsTlCl_3$ and $CsTl_{1-x}Hg_xCl_3$. Theoretical calculations conducted on the In deficient $CsInCl_3$ indicate that it is an indirect band gap semiconductor with a band gap of ∼2.27 eV. The large indirect band gap suggests that this nonstoichiometric perovskite-derived phase is not a good candidate for photovoltaic application. The experimental results, however, provide a basis for future theoretical calculations for designing related inorganic halide perovskites for potential photovoltaic functions or superconductivity.

■ ASSOCIATED CONTENT

Supporting Information

The Supporting Information is available free of charge on the ACS Publications website at DOI: 10.1021/acs.chemmater.8b04771.

EDX spectrum of $Cs_{1.17}In_{0.81}Cl_3$ sample; tilt series of SAED patterns around the c-axis; refined crystallographic data of model I without Cs in In sites; fractional occupancies of sites In2 and In4 as defined by Rietveld refinements of the SXPD; DFT calculation of theoretical and experimental crystal structures of $Cs_{1.17}In_{0.81}Cl_3$ with space group *I4/m*; DFT calculation of Hull energy, energy difference, and existence probability for theoretical and experimental crystal structures of $CsInCl_3$ (PDF)

$Cs_{1.17}In_{0.81}C_{l3}$ (CIF)

■ AUTHOR INFORMATION

Corresponding Authors

*E-mail: kotliar@physics.rutgers.edu (G.K.).
*E-mail: greenbla@chem.rutgers.edu (M.G.).

ORCID

Xiaoyan Tan: 0000-0002-1742-8252
Peter W. Stephens: 0000-0002-8311-7305
Joke Hadermann: 0000-0002-1756-2566
Chang-Jong Kang: 0000-0003-2895-4888
Sun Woo Kim: 0000-0003-1057-2283
Martha Greenblatt: 0000-0002-1806-2766

Present Address

†Department of Chemistry and Biochemistry, George Mason University, Fairfax, Virginia 22030, United States

Notes

The authors declare no competing financial interest.

■ ACKNOWLEDGMENTS

M.G. and X.T. were supported by the Center for Computational Design of Functional Strongly Correlated Materials and Theoretical Spectroscopy under DOE Grant No. DE-FOA-0001276. M.G. also acknowledges support of NSF-DMR-1507252 grant. G.K. and C.-J.K. were supported by the Air Force Office of Scientific Research. MRCAT operations are supported by the Department of Energy and the MRCAT member institutions. The use of the Advanced Photon Source at the Argonne National Laboratory was supported by the U. S. Department of Energy, Office of Science, Office of Basic Energy Sciences, under Contract No. DE-AC02-06CH11357. The works at IOPCAS were supported by NSF & MOST of China through research projects.

■ REFERENCES

(1) Liang, J.; Wang, C.; Wang, Y.; Xu, Z.; Lu, Z.; Ma, Y.; Zhu, H.; Hu, Y.; Xiao, C.; Yi, X.; Zhu, G.; Lv, H.; Ma, L.; Chen, T.; Tie, Z.; Jin, Z.; Liu, J. All-Inorganic Perovskite Solar Cells. *J. Am. Chem. Soc.* **2016**, *138*, 15829−15832.

(2) Jeong, B.; Han, H.; Choi, Y. J.; Cho, S. H.; Kim, E. H.; Lee, S. W.; Kim, J. S.; Park, C.; Kim, D.; Park, C. All-Inorganic $CsPbI_3$ Perovskite Phase-Stabilized by Poly(ethylene oxide) for Red-Light-Emitting Diodes. *Adv. Funct. Mater.* **2018**, *28*, 1706401.

(3) Han, J. S.; Le, Q. V.; Choi, J.; Hong, K.; Moon, C. W.; Kim, T. L.; Kim, H.; Kim, S. Y.; Jang, H. W. Air-Stable Cesium Lead Iodide Perovskite for Ultra-Low Operating Voltage Resistive Switching. *Adv. Funct. Mater.* **2018**, *28*, 1705783.

(4) Vargas, B.; Ramos, E.; Pérez-Gutiérrez, E.; Alonso, J. C.; Solis-Ibarra, D. A Direct Bandgap Copper-Antimony Halide Perovskite. *J. Am. Chem. Soc.* **2017**, *139*, 9116−9119.

(5) Volonakis, G.; Haghighirad, A. A.; Milot, R. L.; Sio, W. H.; Filip, M. R.; Wenger, B.; Johnston, M. B.; Herz, L. M.; Snaith, H. J.; Giustino, F. $Cs_2InAgCl_6$: A New Lead-Free Halide Double Perovskite with Direct Band Gap. *J. Phys. Chem. Lett.* **2017**, *8*, 772−778.

(6) Filip, M. R.; Eperon, G. E.; Snaith, H. J.; Giustino, F. Steric Engineering of Metal-halide Perovskites with Tunable Optical Band Gaps. *Nat. Commun.* **2014**, *5*, 5757.

(7) He, X.; Liu, P.; Zhang, H.; Liao, Q.; Yao, J.; Fu, H. Patterning Multicolored Microdisk Laser Arrays of Cesium Lead Halide Perovskite. *Adv. Mater.* **2017**, *29*, 1604510.

(8) Amgar, D.; Aharon, S.; Etgar, L. Inorganic and Hybrid Organo-Metal Perovskite Nanostructures: Synthesis, Properties, and Applications. *Adv. Funct. Mater.* **2016**, *26*, 8576−8593.

(9) Kovalenko, M. V.; Protesescu, L.; Bodnarchuk, M. I. Properties and Potential Optoelectronic Applications of Lead Halide Perovskite Nanocrystals. *Science* **2017**, *358*, 745−750.

(10) Swarnkar, A.; Marshall, A. R.; Sanehira, E. M.; Chernomordik, B. D.; Moore, D. T.; Christians, J. A.; Chakrabarti, T.; Luther, J. M. Quantum Dot-Induced Phase Stabilization of α-$CsPbI_3$ Perovskite for High-Efficiency Photovoltaics. *Science* **2016**, *354*, 92−95.

(11) Liang, J.; Zhao, P.; Wang, C.; Wang, Y.; Hu, Y.; Zhu, G.; Ma, L.; Liu, J.; Jin, Z. $CsPb_{0.9}Sn_{0.1}IBr_2$ Based All-Inorganic Perovskite Solar Cells with Exceptional Efficiency and Stability. *J. Am. Chem. Soc.* **2017**, *139*, 14009−14012.

(12) Sanehira, E. M.; Marshall, A. R.; Christians, J. A.; Harvey, S. P.; Ciesielski, P. N.; Wheeler, L. M.; Schulz, P.; Lin, L. Y.; Beard, M. C.; Luther, J. M. Enhanced Mobility $CsPbI_3$ Quantum Dot Arrays for Record-Efficiency, High-Voltage Photovoltaic Cells. *Sci. Adv.* **2017**, *3*, eaao4204.

(13) Zhang, L.; Yang, X.; Jiang, Q.; Wang, P.; Yin, Z.; Zhang, X.; Tan, H.; Yang, Y.; Wei, M.; Sutherland, B. R.; Sargent, E. H.; You, J. Ultra-Bright and Highly Efficient Inorganic Based Perovskite Light-Emitting Diodes. *Nat. Commun.* **2017**, *8*, 15640.

(14) Filip, M. R.; Giustino, F. Computational Screening of Homovalent Lead Substitution in Organic−Inorganic Halide Perovskites. *J. Phys. Chem. C* **2016**, *120*, 166−173.

(15) Körbel, S.; Marques, M. A. L.; Botti, S. Stability and Electronic Properties of New Inorganic Perovskites from High-Throughput Ab Initio Calculations. *J. Mater.Chem. C* **2016**, *4*, 3157−3167.

(16) Kang, C.-J.; Kotliar, G. Material Design of Indium-Based Compounds: Possible Candidates for Charge, Valence, and Bond Disproportionation and Superconductivity. *Phys. Rev. Mater.* **2019**, *3*, 015001.

(17) Retuerto, M.; Emge, T.; Hadermann, J.; Stephens, P. W.; Li, M. R.; Yin, Z. P.; Croft, M.; Ignatov, A.; Zhang, S. J.; Yuan, Z.; Jin, C.; Simonson, J. W.; Aronson, M. C.; Pan, A.; Basov, D. N.; Kotliar, G.; Greenblatt, M. Synthesis and Properties of Charge-Ordered Thallium Halide Perovskites, $CsTl^+_{0.5}Tl^{3+}_{0.5}X_3$ (X = F or Cl): Theoretical Precursors for Superconductivity? *Chem. Mater.* **2013**, *25*, 4071−4079.

(18) Cava, R. J.; Batlogg, B.; Krajewski, J. J.; Farrow, R.; Rupp, L. W., Jr.; White, A. E.; Short, K.; Peck, W. F.; Kometani, T. Super-

DOI: 10.1021/acs.chemmater.8b04771
Chem. Mater. 2019, 31, 1981−1989

conductivity near 30 K Without Copper - the $Ba_{0.6}K_{0.4}BiO_3$ Perovskite. *Nature* **1988**, *332*, 814−816.
(19) Climent-Pascual, E.; Ni, N.; Jia, S.; Huang, Q.; Cava, R. J. Polymorphism in $BaPb_{1-x}Bi_xO_3$ at the Superconducting Composition. *Phys. Rev. B* **2011**, *83*, 174512.
(20) Yin, Z. P.; Kutepov, A.; Kotliar, G. Correlation-Enhanced Electron-Phonon Coupling: Applications of GW and Screened Hybrid Functional to Bismuthates, Chloronitrides, and Other High-Tc Superconductors. *Phys. Rev. X* **2013**, *3*, 021011.
(21) Yin, Z. P.; Kotliar, G. Rational Material Design of Mixed-Valent High-Tc Superconductors. *EPL* **2013**, *101*, 27002.
(22) Coehlo, A. A. Topas-Academic V6, http://www.topas-academic.net (accessed February 17, 2019).
(23) Segre, C. U.; Leyarovska, N. E.; Chapman, L. D.; Lavender, W. M.; Plag, P. W.; King, A. S.; Kropf, A. J.; Bunker, B. A.; Kemner, K. M.; Dutta, P.; Duran, R. S.; Kaduk, J. The MRCAT Insertion Device Beamline at the Advanced Photon Source. *CP521, Synchrotron Radiation Instrumentation: Eleventh U.S. National Conference*, P., Pianetta, et al., Eds. American Insitute of Physics: New York, 2000, pp 419-422.
(24) Ravel, B.; Newville, M. ATHENA, ARTEMIS, HEPHAESTUS: Data Analysis for X-ray Absorption Spectroscopy Using IFEFFIT. *J. Synchrotron Radiat.* **2005**, *12*, 537−541.
(25) Newville, M. IFEFFIT : Interactive XAFS Analysis and FEFF Fitting. *J. Synchrotron Radiat.* **2001**, *8*, 322−324.
(26) Wojdyr, M. Fityk: a General-Purpose Peak Fitting Program. *J. Appl. Cryst.* **2010**, *43*, 1126−1128.
(27) Blaha, P.; Schwarz, K.; Madsen, G. K. H.; Kvasnicka, D.; Luitz, J. *WIEN2K, An Augmented Plane Wave + Local Orbitals Program for Calculating Crystal Properties*. Technische Universitët Wien: Wien, Austria, 2001.
(28) Perdew, J. P.; Burke, K.; Ernzerhof, M. Generalized Gradient Approximation Made Simple. *Phys. Rev. Lett.* **1996**, *77*, 3865−3868.
(29) Camargo-Martínez, J. A.; Baquero, R. Performance of the Modified Becke-Johnson Potential for Semiconductors. *Phys. Rev. B* **2012**, *86*, 195106.
(30) Brown, I. D. Recent Developments in the Methods and Applications of the Bond Valence Model. *Chem. Rev.* **2009**, *109*, 6858−6919.
(31) Meyer, G. Zur Kenntnis der Chloro- und Bromo-Indate (III). $A_3In_2Cl_9$ (A = Cs, Rb, In, Tl) und $Cs_3In_2Br_{9-x}Cl_x$ (x = 0, 3, 6, 7, 8). *Z. Anorg. Allg. Chem.* **1978**, *445*, 140−146.
(32) Solans, X.; Moron, M. C.; Palacio, F. Structures of $Rb_2[InCl_5(H_2O)]$ and $Cs_2[InCl_5(H_2O)]$. *Acta Cryst.* **1988**, *C44*, 965−967.
(33) Van Der Vorst, C. P. J. M.; Verschoor, G. C.; Maaskant, W. J. A. The Structures of Yellow and Red Indium Monochloride. *Acta Cryst.* **1978**, *B34*, 3333−3335.
(34) Meyer, G.; Blachnik, R. New Investigations into Mixed-Valence Indium(I, III) Chlorides: The Phase Diagram In/Cl in the 30-50 mole % In Range and the Crystal Structure of In_5Cl_9. *Z. Anorg. Allg. Chem.* **1983**, *503*, 126−132.
(35) Dronskowski, R. Chemical Bonding of the Binary Indium Bromides. *Inorg. Chem.* **1994**, *33*, 6201−6212.
(36) Dronskowski, R. InFeBr3 and InMnBr3: Synthesis, Crystal Structure, Magnetic Properties, and Electronic Structure. *Inorg. Chem.* **1994**, *33*, 5927−5933.
(37) Dronskowski, R. $In_3Ti_2Br_9$: Jahn-Teller Unstable Indium(I) and Antiferromagnetically Coupled Titanium(III) Atoms. *Chem. - Eur. J.* **1995**, *1*, 118−123.
(38) Howard, C. J.; Kennedy, B. J.; Woodward, P. M. Ordered Double Perovskites - a Group-Theoretical Analysis. *Acta Cryst.* **2003**, *B59*, 463−471.
(39) Javier Zúñiga, F.; Tressaud, A.; Darriet, J. The Low-Temperature form of Rb_2KCrF_6 and Rb_2KGaF_6: The First Example of an Elpasolite-Derived Structure with Pentagonal Bipyramid in the B-Sublattice. *J. Solid State Chem.* **2006**, *179*, 3607−3614.
(40) Abakumov, A. M.; King, G.; Laurinavichute, V. K.; Rozova, M. G.; Woodward, P. M.; Antipov, E. V. The Crystal Structure of α-K_3AlF_6: Elpasolites and Double Perovskites with Broken Corner-Sharing Connectivity of the Octahedral Framework. *Inorg. Chem.* **2009**, *48*, 9336−9344.
(41) King, G.; Abakumov, A. M.; Woodward, P. M.; Llobet, A.; Tsirlin, A. A.; Batuk, D.; Antipov, E. V. The high-temperature polymorphs of K_3AlF_6. *Inorg. Chem.* **2011**, *50*, 7792−801.
(42) King, G.; Abakumov, A. M.; Hadermann, J.; Alekseeva, A. M.; Rozova, M. G.; Perkisas, T.; Woodward, P. M.; Van Tendeloo, G.; Antipov, E. V. Crystal Structure and Phase Transitions in Sr_3WO_6. *Inorg. Chem.* **2010**, *49*, 6058−6065.
(43) Stöger, B.; Weil, M.; Zobetz, E. Sr_3TeO_6 and Ba_3TeO_6: Double Perovskites with Pronounced Superstructures. *Z Kristallogr.* **2010**, *225*, 125−138.
(44) Fry, A. M.; Woodward, P. M. Structures of α-$K_3MoO_3F_3$ and α-$Rb_3MoO_3F_3$: Ferroelectricity from Anion Ordering and Noncooperative Octahedral Tilting. *Cryst. Growth. Des.* **2013**, *13*, 5404−5410.
(45) Mandal, T. K.; Poltavets, V. V.; Croft, M.; Greenblatt, M. Synthesis, Structure and Magnetic Properties of $A_2MnB'O6$ (A=Ca, Sr; B′=Sb, Ta) Double Perovskites. *J. Solid State Chem.* **2008**, *181*, 2325−2331.
(46) Ankudinov, A. L.; Ravel, B.; Rehr, J. J.; Conradson, S. D. Real-Space Multiple-Scattering Calculation and Interpretation of X-Ray-Absorption Near-Edge Structure. *Phys. Rev. B* **1998**, *58*, 7565.
(47) Yang, T.; Perkisas, T.; Hadermann, J.; Croft, M.; Ignatov, A.; Van Tendeloo, G.; Greenblatt, M. Synthesis and Structure Determination of Ferromagnetic Semiconductors $LaAMnSnO_6$(A = Sr, Ba). *J. Mater. Chem.* **2011**, *21*, 199−205.
(48) Li, M.-R.; Retuerto, M.; Bok Go, Y.; Emge, T. J.; Croft, M.; Ignatov, A.; Ramanujachary, K. V.; Dachraoui, W.; Hadermann, J.; Tang, M.-B.; Zhao, J.-T.; Greenblatt, M. Synthesis, Crystal Structure, and Properties of $KSbO_3$-type $Bi_3Mn_{1.9}Te_{1.1}O_{11}$. *J. Solid State Chem.* **2013**, *197*, 543−549.
(49) Retuerto, M.; Yin, Z.; Emge, T. J.; Stephens, P. W.; Li, M.-R.; Sarkar, T.; Croft, M. C.; Ignatov, A.; Yuan, Z.; Zhang, S. J.; Jin, C.; Paria Sena, R.; Hadermann, J.; Kotliar, G.; Greenblatt, M. Hole Doping and Structural Transformation in $CsTl_{1-x}Hg_xCl_3$. *Inorg. Chem.* **2015**, *54*, 1066−1075.

DOI: 10.1021/acs.chemmater.8b04771
Chem. Mater. 2019, 31, 1981−1989